Molecular frame photoemission by a comb of elliptical high-order harmonics: a sensitive probe of both photodynamics and harmonic complete polarization state

K. Veyrinas, V. Gruson, Sébastien J. Weber, L. Barreau, T. Ruchon, J.-F. Hergott, J.-C. Houver, R. R. Lucchese, P. Salières, D. Dowek

Title:

Molecular frame photoemission by a comb of elliptical high-order harmonics: a sensitive probe of both photodynamics and harmonic complete polarization state

Authors:

K. Veyrinas, V. Gruson, S. J. Weber, L. Barreau, T. Ruchon, J.-F. Hergott, J.-C. Houver, R. R. Lucchese, P. Salières and D. Dowek

Final manuscript

Journal Name

ARTICLE

Molecular frame photoemission by a comb of elliptical high-order harmonics: a sensitive probe of both photodynamics and harmonic complete polarization state

K. Veyrinas,[a,†] V. Gruson,[b,‡] S. J. Weber,[b,*] L. Barreau,[b] T. Ruchon,[b] J.-F. Hergott,[b] J.-C. Houver,[a] R. R. Lucchese,[c] P. Salières,[b] and D. Dowek[a]

Due to the intimate anisotropic interaction between an XUV light field and a molecule resulting in photoionization (PI), molecular frame photoelectron angular distributions (MFPADs) are most sensitive probes of both electronic/nuclear dynamics and the polarization state of the ionizing light field. Consequently, they encode the complex dipole matrix elements describing the dynamics of the PI transition, as well as the three normalized Stokes parameters s_1, s_2, s_3 characterizing the complete polarization state of the light, operating as molecular polarimetry. The remarkable development of advanced light sources delivering attosecond XUV pulses opens the perspective to visualize the primary steps of photochemical dynamics in time-resolved studies, at the natural attosecond to few femtosecond time-scales of electron dynamics and fast nuclear motion. It is thus timely to investigate the feasibility of measurement of MFPADs when PI is induced e.g., by an attosecond pulse train (APT) corresponding to a comb of discrete high-order harmonics. In the work presented here, we report MFPAD studies based on coincident electron-ion 3D momentum imaging in the context of ultrafast molecular dynamics investigated at the PLFA facility (CEA-SLIC), with two perspectives: i) using APTs generated in atoms/molecules as a source for MFPAD-resolved PI studies, and ii) taking advantage of molecular polarimetry to perform a complete polarization analysis of the harmonic emission of molecules, a major challenge of high harmonic spectroscopy. Recent results illustrating both aspects are reported for APTs generated in unaligned SF_6 molecules by an elliptically polarized infrared driving field. The observed fingerprints of the elliptically polarized harmonics include the first direct determination of the complete s_1, s_2, s_3 Stokes vector, equivalent to (ψ, ε, P), the orientation and the signed ellipticity of the polarization ellipse, and the degree of polarization P. They are compared to -so far- incomplete results of XUV optical polarimetry. We finally discuss the comparison between the outcomes of photoionization and high harmonic spectroscopy for the description of molecular photodynamics.

1. Introduction

Photoionization (PI) is one of the basic processes that allows direct investigation of molecular structure and dynamics; therefore it is often used as a probe of the relaxation of transient excited molecular states involved in gas-phase photochemical dynamics. Resulting from the intimate anisotropic interaction between the light field and a molecule, molecular frame photoelectron angular distributions (MFPADs) are the most sensitive observables of the electronic/nuclear photodynamics induced by

a. Institut des Sciences Moléculaires d'Orsay (ISMO), CNRS, Univ. Paris-Sud, Université Paris-Saclay, F-91405 Orsay, France.
b. LIDYL, CEA, CNRS, Université Paris-Saclay, CEA Saclay, 91191 Gif-Sur-Yvette, France.
c. Department of Chemistry, Texas A&M University, College Station, Texas 77843, USA.
† Present address: Department of Physics, University of Ottawa, 150 Louis Pasteur, Ottawa, Ontario K1N 6N5, Canada.
‡ Present address: INRS, Centre Energie Matériaux et Télécommunications, 1650 Boulevard Lionel-Boulet, Varennes, Quebec, J3X1S2, Canada.
* Present address : CEMES - CNRS, 29 rue Jeanne Marvig, 31055 Toulouse, France.
Electronic Supplementary Information (ESI) available: [details of any supplementary information available should be included here]. See DOI: 10.1039/x0xx00000x

photoionization, *and* they simultaneously encode the polarization state of the ionizing light. Consequently, the determination of MFPADs gives access to the complex dipole matrix elements describing the photoionization transition, as well as to the three normalized Stokes parameters s_1, s_2, s_3 [1] characterizing the complete polarization state of the ionizing light. In particular, the ability to derive s_3, whose sign reflects the light helicity, is a result of the circular dichroism in the molecular frame, i.e., the difference in photoemission when the molecule is exposed to left- or right-handed circularly polarized light. In this work we discuss two ways that the MFPADs can be combined with the use of ultrafast XUV/VUV pulses to contribute to the tool box of Ultrafast Imaging of Photochemical Dynamics.

MFPADs can be accessed using different techniques[2,3], such as photoelectron spectroscopy (PES) applied to rotationally resolved excited molecules or to laser-aligned and oriented molecules, or electron-ion coincidence momentum spectroscopy. In the work presented here we use the latter approach, taking advantage of dissociative photoionization (DPI) of small molecules induced by XUV radiation to determine fully differential MFPADs. On the one hand, this method has provided a wealth of results on the photoionization dynamics following inner-valence shell[4–6] or inner-shell[7–10] ionization of linear molecules or small polyatomic systems most often induced by synchrotron radiation, whose high repetition rate is well appropriate for coincidence measurements, i.e., in the weak field regime. On the other hand, the use of MFPADs as a probe of the complete polarization state of the ionizing light, known as molecular polarimetry (MP)[11], has been benchmarked recently by comparing data relying on coincident electron-ion 3D momentum spectroscopy and on VUV optical polarimetry[12] available on the DESIRS beamline (SOLEIL) which delivers fully controlled VUV elliptically polarized light[13]. This development participates in a substantial effort performed, in particular in the XUV and X-ray domains at large scale facilities such as synchrotrons[12,14] and free electron lasers[15,16], to characterize and control the polarization state of the light source, a key parameter for a number of experiments addressing fundamental topics such as chiral properties of matter[17,18], ranging from biomolecules to magnetic materials. To our knowledge, with the use of optical polarimeters including a dephazer element, the MP method is the only *in situ* approach providing the full determination of the (s_1, s_2, s_3) Stokes vector, equivalent to that of (ψ, ε, P), the orientation and signed ellipticity of the polarization ellipse, *and* the degree of polarization P. In particular, for partially polarized light, the MP method enables us to extract the light helicity s_3 separately from the degree of unpolarized light $s_4 = 1 - P$ (sometimes considered as a fourth Stokes parameter[1]). One clear advantage of the method[11] is its validity across the whole VUV to X-ray range that offers a broad tunability for applications.

The remarkable development of advanced light sources delivering ultrafast XUV pulses has created unprecedented possibilities to address and possibly visualize the primary steps of photochemical dynamics in time-resolved studies of ultrafast processes at the natural time-scale of electron dynamics and fast nuclear motion, ranging from attoseconds to a few femtoseconds. Among these ultrafast sources stand out free electron lasers (FELs), as well as secondary XUV sources based on high-order harmonic generation (HHG), resulting from the non-linear interaction between an intense infrared radiation and a gas medium[19]. Ultrashort coherent XUV pulses may serve two types of application schemes: i) an "external probing" scheme in time-resolved pump-probe PI experiments with controllable delay at the subfemtosecond scale[20–27], and ii) a "self-probing" scheme in the case of HHG, where the three-step generation process (strong field tunnel ionization, laser driven electronic wave-packet motion, and recollision of the returning electron leading to photorecombination)[28,29] probes the system on the time scale of half a laser cycle, a technique now referred to as high harmonic spectroscopy (HHS)[30–35]. In both approaches the molecular frame (MF) observables are a unifying concept for characterizing photochemical dynamics via the snapshot mapping of the electronic density, either in photoemission or by molecular orbital tomography with femto to attosecond temporal resolution. For both approaches too, the occurrence of specific situations where symmetry breaking in the generation process results in the production of elliptically polarized coherent sub-femtosecond pulses has been emphasized in recent experiments, e.g., HHG emission from aligned molecules[36,37] or induced by an elliptical IR laser[38], or HHG driven by a two-color field involving photons of opposite helicity[39]. This context motivates the development of methods for a complete characterization of the harmonic polarization state providing i) sources with optimized ellipticities for time-resolved investigations of dichroisms and ii) access to the complex induced dipole vector and insight into the interactions occurring during the HHG process, in particular the dynamics of the electron-parent ion recombination.

In the work presented here, we report MFPAD studies based on electron-ion coincident 3D momentum spectroscopy in the context of attosecond molecular dynamics conducted at SLIC facility of CEA-Saclay, with the two perspectives addressed above: on the one hand, using the generated APT as a light source for PI of target systems characterized at the MFPAD level[40–42], and on the other hand, taking advantage of MFPAD-resolved PI of simple molecules, to perform a polarization analysis of the HHG emission in high harmonic spectroscopy.

(i) We demonstrate the measurement of complete MFPADs in dissociative photoionization of a chosen molecular target by an attosecond pulse train: this constitutes the first step towards the study of subfemtosecond time-resolved electron/nuclear dynamics in molecules where the reaction launched by the APT is either photoionization, or relaxation of a neutral excited state probed by photoionization, in different pump-probe schemes[43].

(ii) We use the molecular polarimetry to determine the complete polarization state of harmonics generated in SF_6 molecules by an elliptically polarized infrared (IR) field. SF_6 features a polyatomic molecule where it was found that strong field ionization involves contributions from multiple electronic channels, while the recombination step is influenced by resonant transitions due to the presence of autoionizing states and shape resonances[44] trapping the recolliding electron for typically hundreds of attoseconds before recombination to the ground state occurs. Our MP results are compared with data from optical polarimetry (OP) in the conditions of the MP study.

The paper is organized as follows. In order to ensure a self-contained content, we remind in section 2 the general expression of the MFPAD for PI of linear molecules induced by elliptically polarized light, and the subsequent key steps for the extraction of (i) the dynamical parameters of the PI reaction and (ii) the Stokes parameters, providing the grounds for MP. Section 3 describes the experimental methodology, where dissociative photoionization of small molecules induced by an attosecond pulse train is analyzed using 3D-momentum spectroscopy. In section 4, we report the first complete measurements of MFPADs in PI from an incident APT. In section 5, we apply the MP method to the complete characterization of the polarization state of the HH comb produced in SF_6 gas by an elliptically polarized driving laser. Conclusions and perspectives are given in section 6.

2. MFPADs induced by elliptically polarized light: Methodology for molecular polarimetry

The molecular polarimetry method, previously described[11] relies on remarkable properties of molecular frame photoelectron angular distributions (MFPADs) induced by elliptically polarized light[45,46] as obtained in the study of dissociative photoionization (DPI) for primarily linear molecules using electron-ion coincident 3D momentum spectroscopy.

Briefly, for DPI of a molecule AB producing an ion fragment A^+ and a photoelectron, MFPADs are determined from the correlated ion fragment recoil velocity $\mathbf{V_{A+}}$ and photoelectron velocity $\mathbf{V_e}$ measured for each DPI coincident event (A^+,e)[47,48].

$$AB + h\nu(s_1, s_2, s_3) \rightarrow AB^+ + e \rightarrow \mathbf{A^+} + B + \boldsymbol{e} \quad (1)$$

The extension to inner-shell ionization where PI is followed by Auger decay is straightforward[49]. For one-photon PI of a linear molecule, the general expression of the MFPAD in the dipole approximation is a function of three angles, $I(\theta_e, \phi_e, \chi)$, for a linear[50] and circular[45] polarization of the ionizing light, while it is function of an additional angle, $I(\theta_e, \phi_e, \chi, \gamma)$, in the general case where PI is induced by elliptically polarized light[11,46]. (θ_e, ϕ_e) represent the polar and azimuthal electron emission direction in the molecular frame (MF) and (χ, γ) the polar and azimuthal ion fragment emission direction in the field frame (FF) or laboratory frame (LF), as schematized in Figure 1(a). In LF, the z_{LF} reference axis for the (χ) polar dependence is parallel to the $\mathbf{k}$ propagation axis of the ionizing light, with x_{LF} being the reference axis in the polarization plane for the (γ) azimuthal dependence. In MF, z_{MF}, parallel to the ion fragment recoil velocity, i.e., along the molecular axis in the axial recoil approximation, and x_{MF}, unitary vector in the plane containing z_{LF} and z_{MF}, are the reference axes for the (θ_e) and (ϕ_e) polar and azimuthal dependence, respectively. The MP method relies, on the one hand, on the strong dependence of the MFPADs induced by linearly polarized light upon the molecular axis orientation relative to the light polarization axis, and, on the other hand, on the circular dichroism in the MF frame[51] which reflects the different responses of the system when exposed to left (LHC) and right handed circularly (RHC) polarized light, respectively. When PI is induced by elliptically polarized light described by the three Stokes parameters s_1, s_2, s_3, defined in the LF[1], this information is encapsulated in the following analytical form[11,46]:

$$
\begin{aligned}
I(\theta_e, \phi_e, \chi, \gamma) = & F_{00}(\theta_e) + F_{20}(\theta_e)\left[-\frac{1}{2}P_2^0(\cos\chi) + \frac{1}{4}t_1(\gamma)P_2^2(\cos\chi)\right] \\
& + F_{21}(\theta_e)\left\{\left[-\frac{1}{2} - \frac{1}{2}t_1(\gamma)\right]P_2^1(\cos\chi)\cos(\phi_e) - \frac{3}{2}t_2(\gamma)P_1^1(\cos\chi)\sin(\phi_e)\right\} \\
& + F_{22}(\theta_e)\left\{\left[-\frac{1}{2}P_2^2(\cos\chi) + t_1(\gamma)(2 + P_2^0(\cos\chi))\right]\cos(2\phi_e) + 3t_2(\gamma)P_1^0(\cos\chi)\sin(2\phi_e)\right\} \\
& - s_3 F_{11}(\theta_e)P_1^1(\cos\chi)\sin(\phi_e)
\end{aligned} \quad (2)
$$

$$\text{with} \quad t_1(\gamma) = s_1\cos(2\gamma) - s_2\sin(2\gamma)$$
$$t_2(\gamma) = s_1\sin(2\gamma) + s_2\cos(2\gamma)$$

This expression is a generalization of the one describing the MFPAD for circularly polarized light[46], where $t_1(\gamma)$ and $t_2(\gamma)$ average to zero and $s_3 = -1$ for LHC polarization.

Considering equation (2) several conclusions are drawn, which will be used in the following sections:

(i) For any (unknown) polarization of the ionizing light, the four $F_{00}(\theta_e), F_{20}(\theta_e), F_{21}(\theta_e), F_{22}(\theta_e)$ functions can be determined from the Fourier analysis of the $I(\theta_e, \phi_e, \chi)$ measured distribution, ignoring the (γ) dependence, therefore providing the MFPADs for any orientation (χ) of the molecular axis relative to the axis of linearly polarized light[50]. Their (l,λ) partial wave expansion in a Legendre polynomial basis, where l is the angular momentum of the electron in a one center description of the scattering process and the quantum number λ is its projection on the molecular axis, gives access to the complex transition dipole moments describing the parallel and perpendicular PI transitions, and the amplitude of their relative phases. Knowing the sign of these relative phases requires the determination of the $F_{11}(\theta_e)$ function, which appears as the mixed product $s_3 \times F_{11}(\theta_e)$ in the MFPAD expression (Eq.2), as discussed below. Access to these complex transition dipole moments is of high value for the advanced study of the photoemission dynamics.

(ii) The S_1 and S_2 Stokes parameters describing the linear component of the polarization are extracted by a fitting of the $I(\chi, \gamma)$ angular distribution of the ion fragments after integration of the $I(\theta_e, \phi_e, \chi, \gamma)$ angular distribution in (θ_e) and (ϕ_e):

$$I(\chi,\gamma) = C\left[P_0^0\left(\cos\chi\right)\left[1 + \frac{\beta}{2}t_1\left(\gamma\right)\right] - \frac{\beta}{2}P_2^0\left(\cos\chi\right)\left[1 + t_1\left(\gamma\right)\right]\right] \quad (3)$$

The asymmetry parameter of the ion fragment distribution β is obtained from the (χ) dependence after integration in (γ), while the Fourier analysis in (γ) can be performed in the projections on $P_0^0\left(\cos\chi\right)$ and $P_2^0\left(\cos\chi\right)$, providing two ways for extracting s_1 and s_2, as illustrated in Figure 1 (a,b,c):

$$\text{Proj}_{00}(\gamma) = C\left[1 + \frac{\beta}{2}s_1\cos\left(2\gamma\right) - \frac{\beta}{2}s_2\sin\left(2\gamma\right)\right] \text{ and } \text{Proj}_{20}(\gamma) = C'\left[1 + s_1\cos\left(2\gamma\right) - s_2\sin\left(2\gamma\right)\right] \quad (4)$$

We note that a similar form describes the angular distribution of the photoelectrons in the FF, involving the asymmetry parameter of the electron distribution β_e.
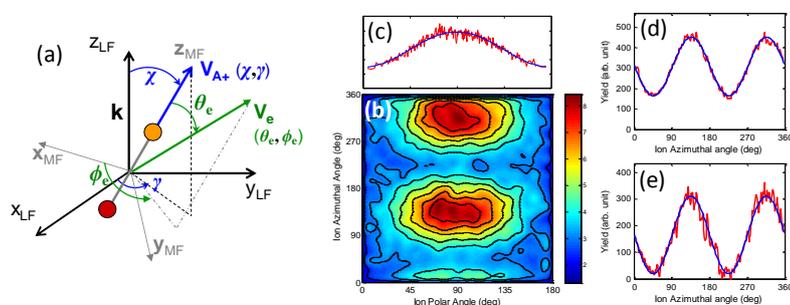
Fig. 1 (a) Schematic of the relevant angles: (θ_e, ϕ_e) represent the polar and azimuthal electron emission direction in the molecular frame (MF) and (χ, γ) the polar and azimuthal ion fragment emission direction in the laboratory frame (LF). (b) $I(\chi, \gamma)$ bidimensional histogram of the (N⁺,e) events showing the ion fragment polar and azimuthal dependence, for the studied polarization state $\mathscr{S}$ at $h\nu$ = 23.65 eV; the 1D plots show (c) the (χ) dependence (d) and (e) the (γ) dependences according to Eqs. (4), providing two determinations of the normalized s_1, s_2 Stokes parameters, i.e., the polarization ellipse orientation angle (ψ) (see Figure 2). The example shown leads to $s_1 = -0.05 \pm 0.01$ and $s_2 = -0.87 \pm 0.01$ corresponding to an orientation $\psi = 133.2° \pm 0.3°$.

(iii) As for the $F_{11}(\theta_e)$ function which characterizes the circular dichroism in the MF, and the S_3 Stokes parameter which features the helicity of the ionizing radiation, they appear as the product $s_3 \times F_{11}(\theta_e)$ in the expression of the MFPAD

$I(\theta_e, \phi_e, \chi, \gamma)$. This implies that determination of $F_{11}(\theta_e)$ requires an independent measurement with a known s_3 helicity, or a calculation. Vice versa, if $F_{11}(\theta_e)$ is known independently, the s_3 Stokes parameter is determined from the MFPAD. It is worth noticing that the MF circular dichroism constitutes the dephasing element of molecular polarimetry. It is also featured by the dimensionless CDAD (circular dichroism in electron angular distribution) parameter, proportional to $F_{11}(\theta_e)$, which characterizes the MF left-right emission asymmetry in the polarization plane (ϕ_e = 90° or 270°) when the molecular axis is perpendicular to the light propagation axis (χ = 90°)[51].

The MP method has been benchmarked using the prototype NO DPI reaction corresponding to ionization of the 4σ inner-valence molecular orbital of the NO(X, $^2\Pi$) molecule (Eq. 5), previously studied[11,45,47], which possesses fingerprint properties to act as an efficient "polarimeter", and is very well adapted to measure the polarization state of HHs composing an APT, as discussed in section 4.

$$NO(^2\Pi, 4\sigma^2 5\sigma^2 1\pi^4 2\pi^1) + h\nu \rightarrow NO^+(c^3\Pi, (4\sigma)^{-1}) + e \rightarrow N^+(^3P) + O(^3P) + e \quad (5)$$

Reaction (5) is the dominant DPI process for the studied XUV photon energies due to a strong shape resonance centered around 30 eV. Dissociation of the $NO^+(c^3\Pi)$ state is prompt relative to the rotational period and satisfies the conditions of axial recoil as validated by the detailed comparison of measured and computed angular anisotropies[45,47]. Both the asymmetry parameter β_{N^+} characterizing the ion fragment emission anisotropy and the MF circular dichroism parameters take significant values ($\beta_{N^+} \approx 1$ and CDAD ranging between 0.5 and 1), which corresponds to favorable conditions for the extraction of the s_1, s_2, s_3 Stokes parameters.

Selecting as an example a polarization state, labelled $\mathscr{S}$, similar to those reported in ref.[11] for a photon energy $h\nu$ = 23.65 eV, Figure 1 displays the key features for the extraction of s_1 and s_2, while Figure 2 illustrates the MF circular dichroism and summarizes the extraction of s_3 leading to the full polarization ellipse.
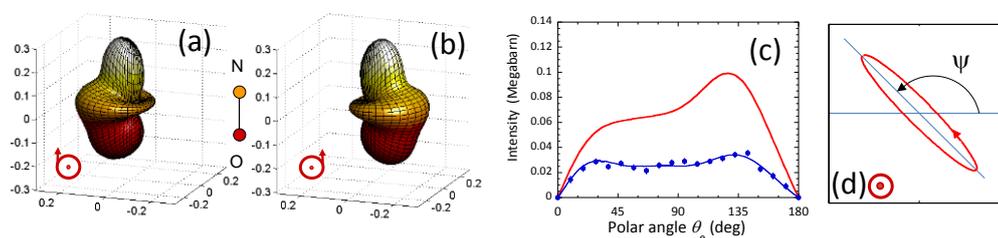
Fig. 2 Illustration of the MF circular dichroism at $h\nu$ = 23.65 eV measured on the DESIRS beamline using circularly polarized light[45]: 3D $I_{90°}(\theta_e, \phi_e)$ MFPADs for $\chi = 90°$ induced by (a) RHC ($s_3 = +1$, helicity -1) and (b) LHC ($s_3 = -1$, helicity +1) polarized light, (c) Extraction of the s_3 Stokes parameter for the $\mathscr{S}$ polarization state: the measured $-s_3 \times F_{11}(\theta_e)$ function is shown (blue: dots and Legendre polynomial line fit); the $s_3 = -0.35 \pm 0.01$ value is obtained here as the ratio between the blue curve and the reference F_{11} function (red), corresponding to an ellipticity $\varepsilon = -0.2 \pm 0.01$. (d) Full polarization ellipse for the $\mathscr{S}$ state, resulting from the measured s_1, s_2, s_3 parameters.

Beside the three Stokes parameters, the polarization state can also be characterized by the parameters of the polarization ellipse which describes the polarized component of the light i.e., the orientation (ψ) and ellipticity (ε)[1], and the degree of polarization P. The (ψ, ε, P) quantities are related to the normalized s_1, s_2, s_3 Stokes parameters as follows:

$$\tan 2\psi = \frac{s_2}{s_1}, \quad \varepsilon = \tan\chi \quad \text{with} \quad \sin 2\chi = \frac{s_3}{\sqrt{s_1^2 + s_2^2 + s_3^2}} \quad \text{and} \quad P = \sqrt{s_1^2 + s_2^2 + s_3^2}$$

$$s_4 = 1 - \sqrt{s_1^2 + s_2^2 + s_3^2} = 1 - P \quad \text{represents the degree of unpolarized light.}$$

For later comparison with OP, we note that incomplete optical measurements relying on the Malus law such as those described in section 3 lead to the determination of the two Stokes parameters (s_1, s_2), equivalent to the ellipse orientation (ψ) and the amplitude of the linear component of the polarization $\sqrt{s_1^2 + s_2^2}$, but do not provide information on the circular and the unpolarised components. One gets only an "upper bound ellipticity" (ε_{ub}) defined as:

$$\varepsilon_{ub} = \tan\chi_{ub} \quad \text{with} \quad \sin 2\chi_{ub} = s_{3-ub}, \quad s_{3-ub} = \sqrt{1 - s_1^2 - s_2^2} \quad \text{and} \quad \varepsilon_{ub} \geq 0$$

ε_{ub} coincides with the absolute value of the ellipticity for fully polarized light $P = 1$, $\varepsilon_{ub} = |\varepsilon|$.

As for the HHG emission, due to the absence of practical XUV dephasing elements, only incomplete optical polarimetry measurements have been performed up to now, assuming a totally polarized light (P=1), thus leading to a possible over estimate of the ellipticity. We point out that the Stokes parameters, as well as the parameters of the polarization ellipse and degree of polarization, are quantities averaged in time and space: they provide an effective description of a temporally and spatially variable field - such as the harmonic field - as the sum of a steadily polarized and unpolarized parts.
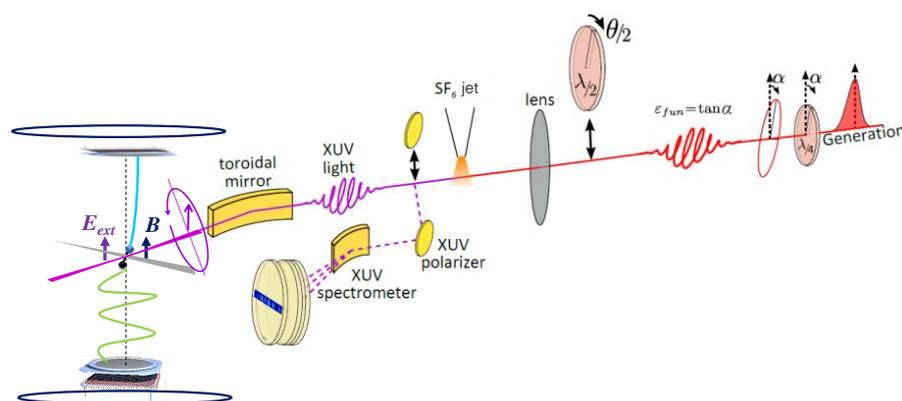
3. Combining 3D-momentum spectrometry with APT generation: experimental methodology

We now turn to the combination of the 3D-momentum spectrometry with APT generation. The experiments have been conducted on the PLFA beamline at SLIC facility of CEA Saclay[52]. A schematic of the setup is shown in Figure 3. The infrared laser delivers pulses at 800 nm with up to 8mJ energy, 50 fs pulse duration at 1 kHz repetition rate. For the SF_6 experiment (Fig. 2a), linearly polarized pulses of about 1mJ are made elliptically polarized through a quarter wave plate whose rotation α determines the signed fundamental ellipticity $\varepsilon_{fun} = \tan(\alpha)$ as well as the direction of the main axis of the ellipse. The IR beam is focused with a 85-cm lens into an effusive gas jet of SF_6 molecules under vacuum. It is then filtered out of the generated harmonics with a 200-nm aluminum foil (not shown). The harmonics are then refocused in the ion-electron coincidence 3D momentum spectrometer CIEL[52] using a 11.5° grazing incidence angle, 22x6 cm size 60-cm focal length toroidal gold mirror. A special care has been taken to characterize the transmission of the polarized harmonics by the toroidal mirror: its action has been calibrated using the MP method, providing s_1, s_2, s_3 Stokes parameters for a series of known linear polarizations of the incident harmonics, that is probing the complex reflectivity for the s and p components for the four studied harmonic energies using Mueller matrix formalism, as briefly discussed in the data analysis of the measured Stokes parameters.

A motorized gold mirror can be inserted upstream from the toroidal mirror. It intersects the light beam at 45° and directs the beam toward a second gold 45°-incidence mirror and an XUV spectrometer (composed of variable groove spacing grating, micro-channel plates and phosphor screen detector). This allows monitoring directly HHG in order to optimize efficiency and beam steering, but also to perform Optical Polarimetry, i.e., Malus' law type polarization analysis using the two 45° reflections as an analyzer. Indeed, the difference of reflectivity between the s and p polarization components amounts to a factor 20 in the 15th-25th harmonic spectral range (23.25-38.75 eV). Instead of turning the analyzer, we use the property that HHG is a field-driven process, the polarization of which in an isotropic target gas is determined by the driving laser. We thus rotate continuously the laser polarization ellipse by an angle θ using a half-wave-plate inserted before the focusing lens, and record the HHG yield $I_q(\theta)$ for the different harmonic orders q on the spectrometer. For a perfect analyzer, this would give the following dependence, also called Malus' law:

$$I_q(\theta) = \frac{1}{2}[S_0 + S_1 \cos(2\theta) + S_2 \sin(2\theta)] \quad (6)$$

The fit of the HHG yield variation with a Malus law taking into account the imperfect analyzer provides the values of the two normalized Stokes parameters: $s_1 = S_1/S_0$ and $s_2 = S_2/S_0$, from which one gets the direction of the harmonic ellipse (ψ), and an upper bound for the magnitude of the ellipticity ε_{ub} (see section 2). Indeed, this incomplete OP cannot disentangle the circular part of the polarization (measured by s_3) from the unpolarized part. Performing a complete OP would require measuring in addition the variation of the HHG yield $I_q(\theta)$ in presence of a dephasing element, like an XUV quarter-wave plate which is not yet available, or using the dephasing induced by reflection on metallic mirror, that comes along with a strong signal attenuation. In most of the published work except for few studies[53,54] the harmonic emission was considered to be fully polarized, so that it was assumed that $\varepsilon_{ub} = |\varepsilon|$.

Fig. 3 Schematic of the experimental set-up combining the HHG PLFA beamline and the electron-ion 3D-momentum spectrometer.

The XUV light beam directed into the CIEL 3D momentum spectrometer induces PI of the gas target, here mainly NO molecular and He atomic targets, produced by a two skimmer supersonic expansion. The supersonic jet and ultrahigh vacuum chambers originate from a previous version of the COLTRIMS type apparatus[55,56] which combines electric and magnetic fields to guide ions and electrons. The advanced version of the spectrometer based on the two delay line time and position sensitive detectors (DLD PSDs RoentDek), including an electrostatic focusing lens for the ion trajectories[48], ensures a 4π collection of both particles, for the studied DPI processes. An eight-channel time-to-digital converter is used to encode the DLD time signals, providing the position for each particle of the (A^+,e) coincident events as well as the ion time of flight (TOF), while the electron TOF is encoded using a synchronized time to amplitude converter.

One issue for the present measurements was the 1 kHz repetition rate of the laser, which restricts to about 50 c/s the overall coincidence count rate. This imposed few hours of stability for each measurement on the NO target. The subsequent statistics for these measurements is discussed in the next sections. This situation has motivated complementary measurements relying on PI of the He target which are not discussed here.

4. MFPADs for PI induced by an attosecond pulse train (APT)

In this section we report the first $I(\theta_e, \phi_e, \chi)$ complete MFPADs subsequent to the interaction of an APT with a molecular target, based on the ($\mathbf{V_{A+}}$, $\mathbf{V_e}$) vector correlation analysis of dissociative photoionization processes. Building on the experience in femtochemistry[57], two strategies have prevailed so far in the few studies of MFPADs in PI of simple molecular targets by attosecond pulses. The first one relies on the impulsive alignment of small molecules such as O_2, N_2, CO, CO_2 using a near-infrared laser and taking advantage of the periodical revival of the rotational wave packet to ionize the molecules at the maximum of field-free alignment or anti-alignment with a properly delayed APT[40]. The energy and $I(\theta_e)$ angular distributions of the photoelectrons were obtained after processing an Abel inversion of the images recorded by Velocity Map Imaging (VMI) and could be assigned to the parallel and perpendicular transitions for the different ionic channels and photon energies in the harmonic comb. Secondly, despite HHG sources usually having rather low repetition rate (1-10 kHz), they allow 3D momentum electron-ion coincidence spectroscopy: first complete measurements of $I(\theta_e, \phi_e, \chi)$ MFPADs were demonstrated in dissociative photoionization of H_2 and D_2 induced by spectrally filtered single high harmonic, following resonant excitation of doubly excited auto-ionizing states[41], and traced as a function of the kinetic energy release of the atomic fragments. This prototypical reaction features a dynamical interplay between the electronic and nuclear motions at the 1-5 femtosecond time scale, giving rise to quantum interferences between distinct reaction pathways and remarkable symmetry breakings, and it stands as a model process for state of the art calculations[58,59]. A related study, based on a similar electron-ion coincidence technique and using a broad band APT, focused on the dependence of photoelectron emission asymmetries in the MF which also illustrates nicely those symmetry breakings[42].

The present study is illustrated by DPI of NO molecules as motivated earlier, and more specifically on the prototype reaction (Eq.5). We use for the ionizing radiation the APT generated by SF_6 molecules driven by elliptically polarized IR laser, the polarization state of which will be characterized using the MP technique in Section 5. Inner-valence ionization of molecules usually involves several DPI processes corresponding to PI into distinct molecular ionic states and dissociation channels, each "reaction pathway" being assigned by the intermediate ionic state and the populated dissociation channel. The first step in the analysis of the (A^+,e) DPI coincident events consists of disentangling the reaction pathways, based on the resolving power of the electron-ion kinetic energy correlation (KEC) featured in KEC diagrams (KECDs)[47,60], and relying on the total energy conservation $(h\nu - \mathrm{E_D} = \mathrm{E_e} + \mathrm{KER})$, where $\mathrm{E_D}$ is the asymptotic potential energy at the dissociation limit, $\mathrm{E_e}$ and KER are the

photoelectron energy and the kinetic energy release of the two heavy atomic/molecular fragments, respectively. Typical KECDs are displayed in Figure 4(a,b) for one-photon PI corresponding to DPI of the NO molecule induced by (a) a one-photon-energy pulse at SOLEIL, here $h\nu$ = 23.65 eV as discussed above and (b) an APT produced by HHG from the SF_6 gas. In Figure 4(a) three DPI processes are identified, which correspond (I) to PI into the first $NO^+(c^3\Pi,(4\sigma)^{-1})$ ionic state followed by dissociation into the $N^+(^3P) + O(^3P) + e$ limit and has the largest intensity, and (II) and (III) to PI into the $NO^+(B^1\Pi,(4\sigma)^{-1})$ and $NO^+(B'^1\Sigma^+,(1\pi)^{-1})$ ionic states dissociating into the $N^+(^3P) + O(^3P) + e$ limit (II) and the two close lying ones $N^+(^1D) + O(^3P) + e$ and/or $N^+(^3P) + O(^1D) + e$ (III)[47].
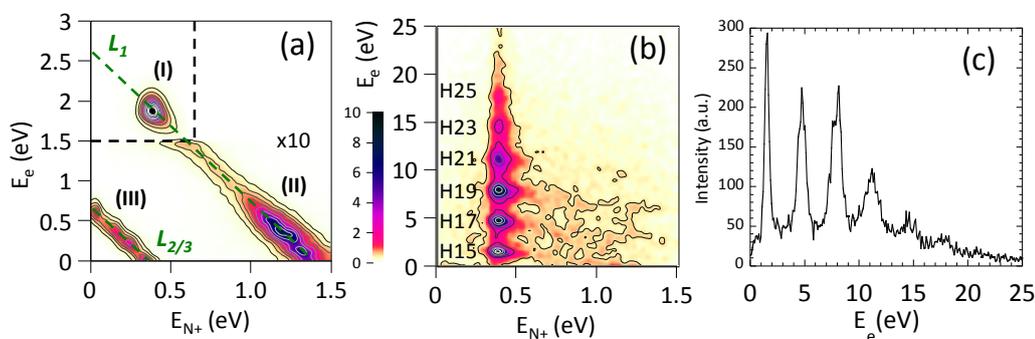

Fig. 4 KECDs characterizing DPI of NO induced by (a) synchrotron radiation at $h\nu$ = 23.65 eV (b) an APT generated on the SF_6 gas medium; (c) Photoelectron spectrum reflecting the HHG spectrum (H15 to H25) convoluted with the PI cross section for Eq.5 (4π collection of electrons and ions) extracted from the KECD shown in (b) after the $0.25\,\text{eV} \leq E_{N+} \leq 0.55\,\text{eV}$ ion-fragment energy selection.

The KECD presented in Figure 4(b) for DPI induced by the APT shows well resolved peaks corresponding to the same $E_{N+} \approx 0.4$ eV ion fragment energy and different E_e electron energies, separated by 3.1 eV, i.e., the energy difference between two successive odd harmonics in the APT. These structures are assigned to the dominant DPI process (Eq.5) produced by the harmonics comb, with energies larger than the ionization potential of NO into the $NO^+(c^3\Pi, v = 0)$ ionic state I$_P$ = 21.7 eV, namely from harmonic H15 up to H25 in the present experiment. Such a KECD reflects the superposition of as many one-photon-energy KECDs as there are contributing HHs in the APT. To ensure a valid interpretation of the KECD assigned to the APT, as well as to provide reference data for the MF circular dichroism at the H15-H23 photon energies, we have performed a series of complementary experiments on the DESIRS beamline at SOLEIL synchrotron using circularly polarized light at the same energies[61,62]. These results establish that there is no significant overlap between the resolved structures assigned to DPI into the $NO^+(c^3\Pi)$ ionic state, and other DPI processes that might result in comparable (E_{N+}, E_e) positions in the KECD, so a proper selection of the processes enable us to proceed to the MFPAD analysis for each harmonic. The reason why weaker processes (II) and (III) resolved in Figure 4(a), or the other DPI processes induced at the higher photon energies, do not provide any significant contribution in Figure 4(b) is, first, the intrinsically weak probability of process (III) and, second, the significant discrimination of processes leading to more energetic N$^+$ fragments at the extraction field chosen for the HHG experiment to ensure a 4π collection of process (I) (Eq.5). Furthermore, scrutiny of the one photon energy KECDs ensures that a unique selection of reaction (Eq.5) induced by the APT is achieved when the $0.25\,\text{eV} \leq E_{N+} \leq 0.55\,\text{eV}$ ion fragment selection is performed. As a result, in the photoelectron spectrum displayed in Figure 4(c) corresponding to this selection, the resolved peaks reflect PI of NO into the $NO^+(c^3\Pi)$ ionic state for each of the HHs composing the APT: it features directly the HHG spectrum for harmonics H15 and higher, convoluted by the total photoionization cross section corresponding to Eq.5. Experimental and/or theoretical PI cross sections can be used as reference to restore the original HHG spectrum[63,64].

Figure 5 displays $I(\theta_e, \phi_e, \chi)$ complete MFPADs, subsequent to the interaction of an APT with the NO molecular target, derived from the measured $I(\theta_e, \phi_e, \chi, \gamma)$ angular distribution for selected processes in the KECD, after integration on the γ angle. Here the APT was generated in SF_6 gas by an elliptically polarized IR laser $\varepsilon_{fun} = 0.2$, the elliptical polarization of the HHs being unknown at this level. Selecting as an example the peak assigned to PI by the H17 harmonic, at photon energy $h\nu$ = 26.35 eV, the complete MFPAD is determined by the extraction of the five $F_{LN}(\theta_e)$ functions implemented in (Eq. 2). The four $F_{00}(\theta_e), F_{20}(\theta_e), F_{21}(\theta_e), F_{22}(\theta_e)$ are displayed in Figure 5(a) providing the $I(\theta_e, \phi_e)$ MFPAD for any orientation of the

molecular axis relative to the axis of linearly polarized light, shown in Figure 5(b) for three meaningful orientations $\chi = 0°, 90°$ featuring the parallel and perpendicular transitions, and $\chi = 45°$, where a coherent superposition between parallel and perpendicular orientations occurs. In Figure 5(a) the $F_{LN}(\theta_e)$ functions are compared with those measured at SOLEIL at photon energy $h\nu$ = 26.35 eV. Despite the rather low statistics in the HHG measurements at the 1 kHz laser rep-rate, reflected by the statistical error bars (e.g. here 3000 events in the selection), the comparison shows that the main characteristics of the MFPADs are fairly well determined. This is a striking demonstration of the potential of the F_{LN}-based data analysis methodology, since all events collected for a given process are used to generate the MFPAD for each selected orientation of the molecule. The 3D plots of the $I(\theta_e, \phi_e)$ MFPADs for the selected orientations illustrate remarkably well the partial wave expansion different for the parallel and perpendicular transitions resulting from the linear combinations of $F_{00}(\theta_e)$ and $F_{20}(\theta_e)$, and including the azimuthal dependence described by the $F_{21}(\theta_e)$ and $F_{22}(\theta_e)$ as soon as the cylindrical symmetry is broken ($\chi \neq 0°$). Expanding the F_{LN} functions in Legendre polynomials enables us to extract the complex dipole matrix elements for the PI transition. Extraction of the $F_{11}(\theta_e)$ function multiplied by the s_3 Stokes parameter, completing the dipole matrix elements, is conveniently presented in the next section where the MP method is applied.
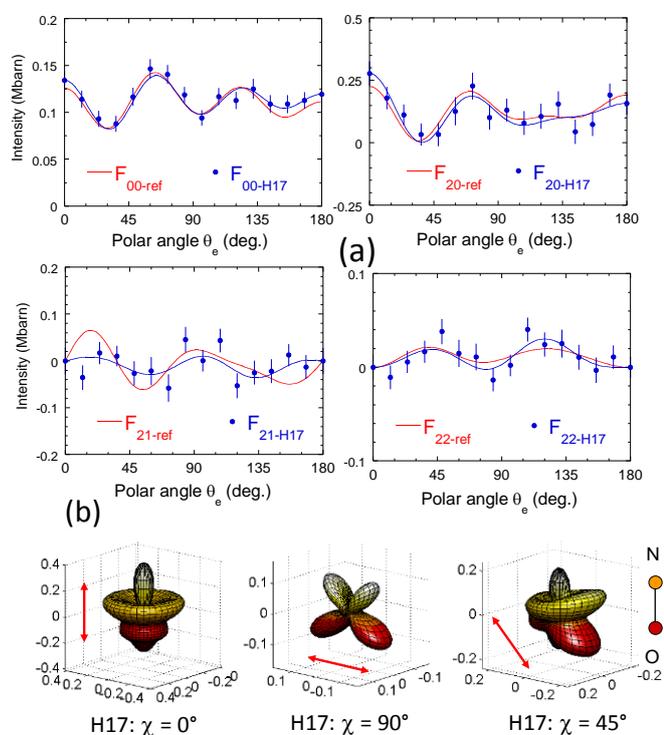

Fig. 5 (a) Measured $F_{00}(\theta_e), F_{20}(\theta_e), F_{21}(\theta_e), F_{22}(\theta_e)$ functions for DPI induced by the harmonic H17 of the APT (blue dots, and Legendre polynomial line fit), compared with the $F_{LN}(\theta_e)$ measured at SOLEIL at $h\nu$ = 26.35 eV (red line); both measurements are normalized to the corresponding MCSCI computed cross section for reaction Eq.5, such that the total cross sections $\int_0^\pi F_{00}(\theta_e) \sin(\theta_e) d\theta_e$ are identical; (b) $I(\theta_e, \phi_e)$ MFPADs for three meaningful orientations $\chi = 0°, 90°$ featuring the parallel and perpendicular transitions, and $\chi = 45°$ involving their coherent superposition. The emission diagram in the MF results from the interference of the $l\lambda$ partial waves building up the electronic wave function in the continuum for the parallel and perpendicular transitions, described by the complex dipole matrix elements. The 3D plots are based on the Legendre polynomial fit of the F_{LN} functions.

As an illustration of the PI dynamics in this region, Figure 6 displays the evolution of the parallel transition with the HH order, scanning the photon excitation energy across the σ* shape resonance of the $NO^+(c^3\Pi)$ ionization channel[45,64], very well predicted by multichannel Schwinger configuration interaction method (MCSCI) when the effects of the dynamic electronic correlation, i.e., the correlated motion of the photoelectron and electrons of the target are included[45,50]. The dominance of the *f* partial wave and the π increase of the phases of the matrix elements can therefore be discussed in this context where significant interchannel coupling occurs. At the maximum of the shape resonance, around 30 eV, i.e. H19, it leads to a strong electron emission anisotropy, favoring electron ejection along the molecular axis in the direction of the O end of the NO molecule.
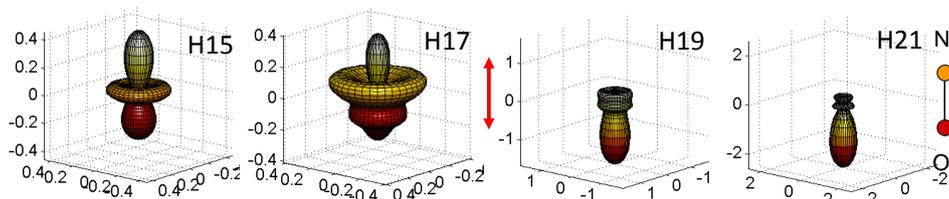
Fig. 6 Evolution of the $I(\theta_e)$ MFPAD for the $\chi = 0°$ orientation, featuring the parallel transition, across the energy region scanned by the H15-H21 harmonics, corresponding to the shape resonance of the $NO^+(c^3\Pi)$ ionic state. The 3D plots are based on the Legendre polynomial fit of the measured F_{LN} functions (see Fig. 5).

These results open perspectives for time-resolved MFPAD studies at the attosecond time scale, with the goal to probe the evolution of e.g., the electronic density in a transient excited molecular state through photoionization. At the same time, the fast and striking evolution of the MFPAD along the shape resonance shown in Fig.6 illustrates the important role of the PI dynamics, i.e., here the influence of the electron-ion scattering process including dynamic electronic correlation.

## 5. Molecular polarimetry: an *in situ* tool for polarization analysis in high-order harmonic spectroscopy (HHS)

High-harmonic spectroscopy of unaligned SF$_6$ molecules[38,44,65] pertains to recent experimental and theoretical studies aiming at the extension of this ultrafast metrology to polyatomic molecules[32,66–70], with a focus on the role of non-adiabatic multi-electron dynamics and coherent superposition of multiple channels. Different HHS methods were combined to characterize HHG from the SF$_6$ generation medium[44], among which the investigation of the spectral dependence of the parameters describing the polarization ellipse of the XUV harmonics. Optical polarimetry measurements based on the Malus' law, in terms of the ellipse orientation and the upper bound ellipticity ε_{ub}, showed unprecedented values ranging between 0.8 and 0.6 for harmonics H13 to H17 for an ellipticity $\varepsilon_{fun} = 0.2$ of the 800 nm driving laser[38]. The produced elliptically polarized HHG source was subsequently used to measure photoelectron circular dichroism (PECD)[71] on chiral molecules[38], i.e., to characterize the electron emission forward/backward asymmetry along the propagation direction of the light. Such measurements should provide the s_3 Stokes parameter, if the PECD is calibrated independently and if the contribution of each HH can be resolved in the photoelectron spectra.

We applied the MP method to the analysis of the APT generated in SF$_6$ by an elliptically polarized driving IR laser, with the goal of probing the complete polarization state of each HH composing the APT, expressed in terms of the s_1, s_2, s_3 Stokes parameters, or the (ψ, ε, P) quantities characterizing the polarization ellipse and the degree of polarization *P*. The analysis of the measured $I(\chi, \gamma)$ histograms and the $s_3 \times F_{11}(\theta_e)$ functions for the four DPI processes induced by the H15-H21 major harmonics proceeds along the lines described in section 2.

For the extraction of the s_3 Stokes parameters, we rely on the reference $F_{11}(\theta_e)$ functions which were measured on the DESIRS beamline at SOLEIL at the same photon energies[62], and are well predicted by MCSCI calculations[45]: for each harmonic, the s_3 value is obtained as the ratio between the $s_3 \times F_{11}(\theta_e)$ curve and the reference $F_{11}(\theta_e)$ function at the corresponding photon energy. s_1 and s_2 are derived from the analysis of the $I(\chi, \gamma)$ histograms for each harmonic according to the method illustrated in Figure 1.

ARTICLE

However one additional step has to be included in the data analysis, which accounts for the modification of the polarization state of the HHGs which is likely to be introduced by optical elements, in particular the toroidal gold mirror which focuses the XUV pulses at the center of the COLTRIMS spectrometer. As mentioned in the experimental section, the action of this mirror has been characterized using the MP method, providing s_1, s_2, s_3 Stokes for a series of known orientations of the incident linearly polarized XUV field (i.e., that of the infrared laser), and modeled with a designed Mueller matrix which includes transmission parameters for the four relevant harmonics. The other optical element crossed by the XUV pulses is the metallic Al filter which has a flat response in the region of interest and should not influence the polarization state. In the data reported in the following the Mueller formalism was used to determine the complete polarization state for each harmonic in terms of the normalized Stokes vector upstream from the mirror, based on that directly measured after transmission by the mirror.

Figure 7 illustrates the extraction of the s_3 Stokes parameters for the four harmonics downstream from the mirror: the MFPADs display significant right-left asymmetries which demonstrate that large positive s_3 values are obtained, in particular for H15 and H17.

$$s_3 = +0.66 \qquad s_3 = +0.76 \qquad s_3 = +0.53 \qquad s_3 = +0.42$$
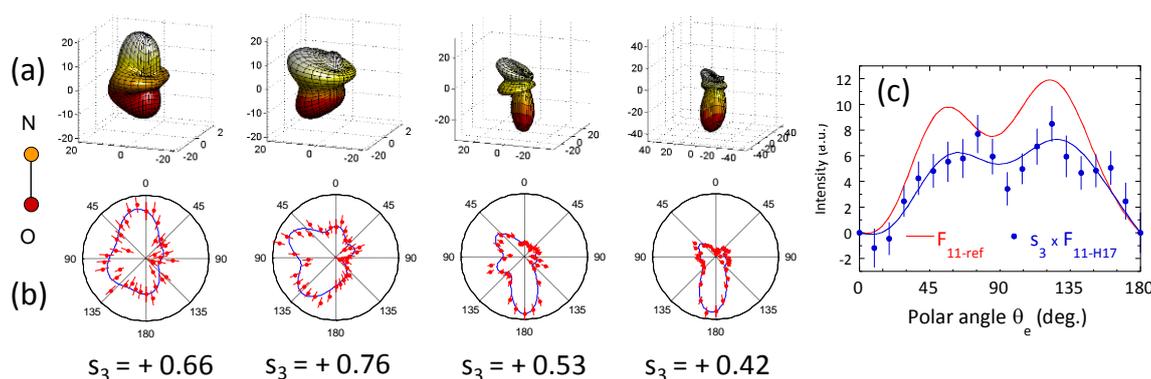
Fig. 7 (a) $I(\theta_e, \phi_e)$ MFPADs for the $(\chi = 90°)$ orientation of the molecular axis relative to the propagation axis of the APT generated by $\varepsilon_{fun} \approx 0.23$ of the driving IR laser, for the H15 to H21 harmonics: the significant right-left emission anisotropies reflect the HH dependent s_3 Stokes parameter and F_{11} function (b) Cuts of the MFPADs in the polarization plane (ϕ_e = 90° or 270°) displaying the largest CDAD anisotropy (c) s_3 x $F_{11}(\theta_e)$ for H17 (blue dots and Legendre polynomial fit line) compared to the reference F_{11} function at $h\nu$ = 26.35 eV (red line): the $s_3 = 0.76 \pm 0.05$ value is obtained as the ratio between the blue curve and the reference F_{11} function (red); the measured values downstream from the mirror are shown at the bottom of the figure, with ± 0.05 error bars, while the values upstream from the mirror amount to $s_3 = 0.78, 0.77, 0.51,$ and $0.22 (\pm 0.05)$, respectively, using the Mueller formalism (see text).

The large values determined for the s_3 Stokes parameter, in particular $s_3 \approx 0.8 \pm 0.05$ for H15 and H17, demonstrate unambiguously the large degree of polarization and the quasi-circular character of the polarization state for these harmonics, corresponding to a positive ellipticity $\varepsilon \approx 0.70 \pm 0.06$. For H19 and H21 the sign remains positive while the magnitude of the ellipticity decreases.

In Figure 8 we present the results obtained with the MP method for two ε_{fun} values of opposite sign close to $\varepsilon_{fun} \approx \pm 0.2$ (which we would rather attribute to $\varepsilon_{fun} \approx 0.23$ and $\varepsilon_{fun} \approx -0.17$ in the MP measurement), in terms of the polarization ellipse parameters, orientation (ψ) and ellipticity (ε), as well as the degree of polarization P. Figure 8 also includes the results of optical polarimetry based on Malus' law obtained at SLIC-PLFA in terms of the orientation (ψ) and the upper bound value ε_{ub}.
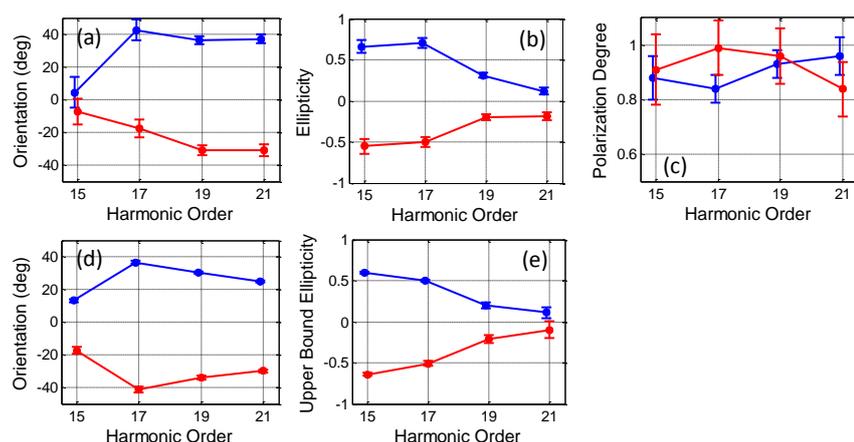
Fig. 8 First row: MP (a) Orientation of the polarization ellipse (ψ) relative to the reference direction of the driving IR laser (b) measured ellipticity (ε) (c) polarization degree, for $\varepsilon_{fun} \approx 0.23$ (blue dots) and $\varepsilon_{fun} \approx -0.17$ (red dots).

Second row: OP (d) Orientation of the polarization ellipse (ψ) relative to that of the driving IR laser (e) ε_{ub} (affecting artificially a negative sign to facilitate the visualization of the result), for $\varepsilon_{fun} \approx 0.2$ (blue dots) and $\varepsilon_{fun} \approx -0.2$ (red dots).

The orientation displayed in Fig. 8(a) as a function of the harmonic order, derived from the values of s_1 and s_2, strongly increases from about 5° to 40° from H15 to H17 for $\varepsilon_{fun} \approx 0.23$, and then remains rather stable. A quasi-symmetric behavior is observed for $\varepsilon_{fun} \approx -0.17$. The main trend is in good agreement with the variation shown by the PLFA-OP results in Fig. 8(d), displaying smaller error bars than the MP ones for statistical issues inherent to the present MP experiment. It compares fairly well with the previous OP measurements of (ψ) reported by Ferré et al.[38,44], although we do not observe in the MP and PLFA-OP data the reported sign change of the orientation angle between H15 et H17: this might be attributed to the "quasi-circular" polarization at such HH energies, where the ellipse orientation nearly vanishes leading to larger uncertainties in its determination, or to the high sensitivity of the polarization characteristics to the generation conditions, e.g. a different detuning from resonances in this energy region. As noted above, measuring s_3, in addition to s_1 and s_2, provides an unambiguous determination of the ellipticity of each HH, including its sign, ranging here from $\varepsilon \approx 0.70 \pm 0.06$ for H15 and H17 down to $\varepsilon \approx 0.31 \pm 0.03$ and $\varepsilon \approx 0.12 \pm 0.04$ for H19 and H21, for $\varepsilon_{fun} \approx 0.23$. This demonstrates that the large ε_{ub} found for H15 and H17 in OP reported by Ferré et al.[38,44], and presently measured at SLIC-PLFA, is indeed due to the high degree of ellipticity of the polarization and not to a significant depolarization for these HHs.

The polarization degree shows, for the case $\varepsilon_{fun} \approx 0.23$, some deviation from the maximum value of 1 for the resonant harmonics 15 and 17, although with big error bars. The case $\varepsilon_{fun} \approx -0.17$ does not show this trend, which could possibly be due to an unprecision in the determination of s_1 and s_2, in particular for H17. A higher repetition rate in future experiments will allow increasing the statistics and thus reducing these error bars in order to reach final conclusion on the presence of depolarization in this case.

These polarization characteristics are providing insight into the complex interactions occurring during the HHG process in the SF_6 molecule. It was proposed[44] that the first step, i.e., strong field ionization involves contributions from multiple electronic channels, while the recombination step is influenced by resonant transitions due to the presence of autoionizing states and shape resonances trapping the recolliding electron for typically hundreds of attoseconds before recombination to the ground state occurs. The specific behavior observed for H15 and H17 was related to the presence of the $5t_{1u} \rightarrow \varepsilon t_{2g}$ shape resonance in the A channel that dominates the harmonic emission in this spectral range, as shown by complex Kohn computations of valence PI total cross sections involving strong intercoupling effects[72]. The influence of resonances was then investigated using 2D-TDSE simulations for Ar atoms (see the supplementary information of [38]), and it was found that they result in a structuring of the returning electron wavepacket and an increase of the perpendicular component of the dipole in the radiative recombination step of the HHG process. The high ε_{ub} values (assimilated to (ε)) measured in SF_6 were then attributed to such an effect induced by $5t_{1u} \rightarrow \varepsilon t_{2g}$ shape resonance. The reported MP measurements prove that the harmonic emission is indeed highly elliptical, which strengthens the proposed interpretation in terms of resonance. Furthermore, some degree of depolarization is expected in such

a case, because the polarization characteristics should be highly dependent on the detuning from the resonance, inducing spectral variations inside the harmonic bandwidth[38]. This calls for more precise MP measurements using a high repetition rate laser. With the direct determination of the signed ellipticity and of the degree of polarization, these results complement those obtained previously for SF_6 and demonstrate the potential of the MP method to access the complete state of polarization of the HHs composing an APT. The interpretation of the striking fingerprints of the ε_{fun} and harmonic order dependent polarization state of the HHs composing the APT generated on SF_6 molecules, in particular the large ellipticities and strong variation of the ellipse orientation in the H13-H17 range, calls for additional theoretical studies.

6. Conclusion

In the work presented we have reported MFPAD studies based on coincident electron-ion 3D momentum imaging in the context of ultrafast molecular dynamics investigated at the SLIC facility of CEA-Saclay, with two perspectives, namely i) using APT generated in atoms/molecules as a source for PI studies performed at the level of MFPADs, and ii) taking advantage of MFPAD-resolved PI of simple molecules to perform a polarization analysis of the HHG emission in molecules, a major challenge of high harmonic spectroscopy.

The ability to measure $I(\theta_e, \phi_e, \chi)$ complete MFPADs induced by an APT opens perspectives for two-color pump-probe time-resolved MFPAD studies at the attosecond time scale, with the goal to probe the evolution of e.g., the electronic density in a transient excited molecular state through photoionization. Entangled with the intrinsic properties of the ionized molecular orbital, the PI dynamics at play during the electron-ion scattering process has major impact on MFPAD. This points to the need for a thorough description of the PI processes, as aimed by different ab initio theoretical approaches.

This direction calls for extensions of the F_{LN} based method for extraction of the MFPADs to a two(multi)- photon PI process (pump-probe) on the one hand, as well as to non-linear small polyatomic molecules, providing then recoil frame photoelectron angular distributions (RFPADs), on the other hand. This type of extension was discussed recently for e.g., the description of DPI of the NO_2 molecule induced by one-photon[73] and multi-photon[74] absorption. The vibrational dynamics at conical intersections, electronic correlations and quantum interferences, or isomerization reactions, are e.g., some of the key processes which can be advantageously studied at the detailed level of time-resolved RFPADs both experimentally and theoretically in small model molecular systems[43].

In this work, the MP method has been applied to the complete determination of the polarization state of the harmonic comb in APTs generated in SF_6 molecules by an elliptically polarized driving field. We have investigated two other cases where symmetry breaking in the generation process results in the production of elliptically polarized harmonics, well identified in recent literature, namely HHG driven by two color counter rotating circularly polarized fields in Ar atoms, and HHG driven by linearly polarized light in aligned N_2 molecules [in preparation]. One outcome and issue of these first results is the evaluation of depolarization of the generated HHs, in particular in the study of HHG from aligned molecules. It raises interesting questions on the different possible origins of depolarization[53,54], which will be addressed in future work.

Both above perspectives (i) and (ii) will be pursued, taking advantage of the current development of high repetition rate (> 1 kHz) HHG sources for future experiments, such as the 10 kHz FAB10 ATTOLAB source, allowing a significant increase of the statistics.

Finally, the investigation of MFPADs or RFPADs induced by an APT contributes to the ongoing comparison between PI and HHS studies, i.e., the complementary insights on photoinitiated ultrafast electronic and nuclear dynamics in molecules which can be extracted from the two approaches, respectively. In PI, the $I(\theta_e, \phi_e, \chi)$ MFPAD describing photoelectron emission at the microscopic level gives the most complete access to the partial wave resolved complex dipole matrix elements, at each photon energy. On the other hand, in a gas medium HHS observables build up coherently from the microscopic to the macroscopic level, under condition of phase-matching between the nonlinear polarization and the harmonic field.

Gathering theoretical concepts relevant for HHG and PI, the quantitative rescattering theory (QRS) for linear aligned molecules[75,76] and unaligned polyatomic molecules[66] provides an illustrative theoretical framework for the description of the HHG process, where the photorecombination step is considered as time-reversed PI. Strengthening the fruitful combination of thorough MFPAD-PI and HHS studies, both in experiments and theory, should provide more insight into the specificities of the strong-field driven dynamics in HHG beyond the QRS theory (see [77] and references therein).

Acknowledgements

Notes and references

1   M. Born and E. Wolf, *Principles of Optics*, Pergamon, New York, 1980.
2   K. L. Reid, *Mol. Phys.*, 2012, **110**, 131–147.
3   Special issue on molecular-frame photoelectron angular distributions, J. Phys. B At. Mol. Opt. Phys.,2012, 45, Issue 19.
4   S. Motoki, J. Adachi, K. Ito, K. Ishii, K. Soejima, A. Yagishita, S. K. Semenov and N. A. Cherepkov, *Phys. Rev. Lett.*, 2002, **88**, 63003.
5   O. Geßner, Y. Hikosaka, B. Zimmermann, A. Hempelmann, R. R. Lucchese, J. H. D. Eland, P.-M. Guyon and U. Becker, *Phys. Rev. Lett.*, 2002, **88**, 193002.
6   M. Lebech, J. C. Houver, D. Dowek and R. R. Lucchese, *Phys. Rev. Lett.*, 2006, **96**, 73001.
7   A. Landers, T. Weber, I. Ali, A. Cassimi, M. Hattass, O. Jagutzki, A. Nauert, T. Osipov, A. Staudte, M. H. Prior, H. Schmidt-Böcking, C. L. Cocke and R. Dörner, *Phys. Rev. Lett.*, 2001, **87**, 13002.
8   T. Jahnke, T. Weber, A. L. Landers, A. Knapp, S. Schössler, J. Nickles, S. Kammer, O. Jagutzki, L. Schmidt, A. Czasch, T. Osipov, E. Arenholz, A. T. Young, R. Díez Muiño, D. Rolles, F. J. García de Abajo, C. S. Fadley, M. A. Van Hove, S. K. Semenov, N. A. Cherepkov, J. Rösch, M. H. Prior, H. Schmidt-Böcking, C. L. Cocke and R. Dörner, *Phys. Rev. Lett.*, 2002, **88**, 73002.
9   T. Osipov, T. N. Rescigno, T. Weber, S. Miyabe, T. Jahnke, A. S. Alnaser, M. P. Hertlein, O. Jagutzki, L. P. H. Schmidt, M Schöffler, L. Foucar, S. Schössler, T. Havermeier, M. Odenweller, S. Voss, B. Feinberg, A. L. Landers, M. H. Prior, R Dörner, C. L. Cocke and A. Belkacem, *J. Phys. B At. Mol. Opt. Phys.*, 2008, **41**, 91001.
10 X.-J. Liu, H. Fukuzawa, T. Teranishi, A. De Fanis, M. Takahashi, H. Yoshida, A. Cassimi, A. Czasch, L. Schmidt, R. Dörner, K. Wang, B. Zimmermann, V. McKoy, I. Koyano, N. Saito and K. Ueda, *Phys. Rev. Lett.*, 2008, **101**, 83001.
11 K. Veyrinas, C. Elkharrat, S. Marggi Poullain, N. Saquet, D. Dowek, R. R. Lucchese, G. A. Garcia and L. Nahon, *Phys. Rev. A*, 2013, **88**, 063411.
12 L. Nahon and C. Alcaraz, *Appl. Opt.*, 2004, **43**, 1024–1037.
13 L. Nahon, N. de Oliveira, G. A. Garcia, J.-F. Gil, B. Pilette, O. Marcouillé, B. Lagarde and F. Polack, *J. Synchrotron Radiat.*, 2012, **19**, 508–520.
14 F. Schäfers, H.-C. Mertins, A. Gaupp, W. Gudat, M. Mertin, I. Packe, F. Schmolla, S. Di Fonzo, G. Soullié, W. Jark, R. Walker, X. Le Cann, R. Nyholm and M. Eriksson, *Appl. Opt.*, 1999, **38**, 4074–4088.
15 E. Allaria, B. Diviacco, C. Callegari, P. Finetti, B. Mahieu, J. Viefhaus, M. Zangrando, G. De Ninno, G. Lambert, E. Ferrari, J. Buck, M. Ilchen, B. Vodungbo, N. Mahne, C. Svetina, C. Spezzani, S. Di Mitri, G. Penco, M. Trovó, W. M. Fawley, P. R. Rebernik, D. Gauthier, C. Grazioli, M. Coreno, B. Ressel, A. Kivimäki, T. Mazza, L. Glaser, F. Scholz, J. Seltmann, P. Gessler, J. Grünert, A. De Fanis, M. Meyer, A. Knie, S. P. Moeller, L. Raimondi, F. Capotondi, E. Pedersoli, O. Plekan, M. B. Danailov, A. Demidovich, I. Nikolov, A. Abrami, J. Gautier, J. Lüning, P. Zeitoun and L. Giannessi, *Phys. Rev. X*, 2014, **4**, 41040.
16 T. Mazza, M. Ilchen, A. J. Rafipoor, C. Callegari, P. Finetti, O. Plekan, K. C. Prince, R. Richter, M. B. Danailov, A. Demidovich, G. De Ninno, C. Grazioli, R. Ivanov, N. Mahne, L. Raimondi, C. Svetina, L. Avaldi, P. Bolognesi, M. Coreno, P. O'Keeffe, M. Di Fraia, M. Devetta, Y. Ovcharenko, T. Möller, V. Lyamayev, F. Stienkemeier, S. Düsterer, K. Ueda, J. T. Costello, A. K. Kazansky, N. M. Kabachnik and M. Meyer, *Nat. Commun.*, 2014, **5**, 3648.
17 L. D. Barron, *Molecular Light Scattering and Optical Activity*, Cambridge University Press, Cambridge, England, 2004.
18 N. Berova, K. Nakanishi and R. Woody, *Circular Dichroism: Principles and Applications*, Wiley-VCH, New York, 2000.
19 F. Krausz and M. Ivanov, *Rev. Mod. Phys.*, 2009, **81**, 163–234.
20 Y. H. Jiang, A. Rudenko, O. Herrwerth, L. Foucar, M. Kurka, K. U. Kühnel, M. Lezius, M. F. Kling, J. van Tilborg, A. Belkacem, K. Ueda, S. Düsterer, R. Treusch, C. D. Schröter, R. Moshammer and J. Ullrich, *Phys. Rev. Lett.*, 2010, **105**, 263002.
21 J. Ullrich, A. Rudenko and R. Moshammer, *Annu. Rev. Phys. Chem.*, 2012, **63**, 635–660.
22 B. Erk, R. Boll, S. Trippel, D. Anielski, L. Foucar, B. Rudek, S. W. Epp, R. Coffee, S. Carron, S. Schorb, K. R. Ferguson, M. Swiggers, J. D. Bozek, M. Simon, T. Marchenko, J. Küpper, I. Schlichting, J. Ullrich, C. Bostedt, D. Rolles and A. Rudenko, *Science*, 2014, **345**, 288–291.
23 R. Boll, A. Rouzée, M. Adolph, D. Anielski, A. Aquila, S. Bari, C. Bomme, C. Bostedt, J. D. Bozek, H. N. Chapman, L. Christensen, R. Coffee, N. Coppola, S. De, P. Decleva, S. W. Epp, B. Erk, F. Filsinger, L. Foucar, T. Gorkhover, L. Gumprecht, A. Hömke, L. Holmegaard, P. Johnsson, J. S. Kienitz, T. Kierspel, F. Krasniqi, K.-U. Kühnel, J. Maurer, M. Messerschmidt, R. Moshammer, N. L. M. Müller, B. Rudek, E.

Savelyev, I. Schlichting, C. Schmidt, F. Scholz, S. Schorb, J. Schulz, J. Seltmann, M. Stener, S. Stern, S. Techert, J. Thøgersen, S. Trippel, J. Viefhaus, M. Vrakking, H. Stapelfeldt, J. Küpper, J. Ullrich, A. Rudenko and D. Rolles, *Faraday Discuss.*, 2014, **171**, 57–80.

24 M. Drescher, M. Hentschel, R. Kienberger, M. Uiberacker, V. Yakovlev, A. Scrinzi, T. Westerwalbesloh, U. Kleineberg, U. Heinzmann and F. Krausz, *Nature*, 2002, **419**, 803–807.

25 S. Gilbertson, S. D. Khan, Y. Wu, M. Chini and Z. Chang, *Phys. Rev. Lett.*, 2010, **105**, 93902.

26 G. Sansone, F. Kelkensberg, J. F. Pérez-Torres, F. Morales, M. F. Kling, W. Siu, O. Ghafur, P. Johnsson, M. Swoboda, E. Benedetti, F. Ferrari, F. Lépine, J. L. Sanz-Vicario, S. Zherebtsov, I. Znakovskaya, A. L'Huillier, M. Y. Ivanov, M. Nisoli, F. Martín and M. J. J. Vrakking, *Nature*, 2010, **465**, 763–766.

27 A. Wirth, M. T. Hassan, I. Grguraš, J. Gagnon, A. Moulet, T. T. Luu, S. Pabst, R. Santra, Z. A. Alahmed, A. M. Azzeer, V. S. Yakovlev, V. Pervak, F. Krausz and E. Goulielmakis, *Science*, 2011, **334**, 195–200.

28 P. B. Corkum, *Phys. Rev. Lett.*, 1993, **71**, 1994–1997.

29 K. J. Schafer, B. Yang, L. F. DiMauro and K. C. Kulander, *Phys. Rev. Lett.*, 1993, **70**, 1599–1602.

30 J. Itatani, J. Levesque, D. Zeidler, H. Niikura, H. Pépin, J. C. Kieffer, P. B. Corkum and D. M. Villeneuve, *Nature*, 2004, **432**, 867–871.

31 S. Haessler, J. Caillat, W. Boutu, C. Giovanetti-Teixeira, T. Ruchon, T. Auguste, Z. Diveki, P. Breger, A. Maquet, B. Carré, R. Taïeb and P. Salières, *Nat. Phys.*, 2010, **6**, 200–206.

32 O. Smirnova, Y. Mairesse, S. Patchkovskii, N. Dudovich, D. Villeneuve, P. Corkum and M. Y. Ivanov, *Nature*, 2009, **460**, 972–977.

33 C. Vozzi, M. Negro, F. Calegari, G. Sansone, M. Nisoli, S. De Silvestri and S. Stagira, *Nat. Phys.*, 2011, **7**, 822–826.

34 N. L. Wagner, A. Wüest, I. P. Christov, T. Popmintchev, X. Zhou, M. M. Murnane and H. C. Kapteyn, *Proc. Natl. Acad. Sci.*, 2006, **103**, 13279–13285.

35 H. J. Wörner, J. B. Bertrand, B. Fabre, J. Higuet, H. Ruf, A. Dubrouil, S. Patchkovskii, M. Spanner, Y. Mairesse, V. Blanchet, E. Mével, E. Constant, P. B. Corkum and D. M. Villeneuve, *Science*, 2011, **334**, 208–212.

36 X. Zhou, R. Lock, N. Wagner, W. Li, H. C. Kapteyn and M. M. Murnane, *Phys. Rev. Lett.*, 2009, **102**, 73902.

37 Y. Mairesse, J. Higuet, N. Dudovich, D. Shafir, B. Fabre, E. Mével, E. Constant, S. Patchkovskii, Z. Walters, M. Y. Ivanov and O. Smirnova, *Phys. Rev. Lett.*, 2010, **104**, 213601.

38 A. Ferré, C. Handschin, M. Dumergue, F. Burgy, A. Comby, D. Descamps, B. Fabre, G. A. Garcia, R. Géneaux, L. Merceron, E. Mével, L. Nahon, S. Petit, B. Pons, D. Staedter, S. Weber, T. Ruchon, V. Blanchet and Y. Mairesse, *Nat. Photonics*, 2015, **9**, 93–98.

39 O. Kfir, P. Grychtol, E. Turgut, R. Knut, D. Zusin, D. Popmintchev, T. Popmintchev, H. Nembach, J. M. Shaw, A. Fleischer, H. Kapteyn, M. Murnane and O. Cohen, *Nat. Photonics*, 2015, **9**, 99–105.

40 A. Rouzée, F. Kelkensberg, W. K. Siu, G. Gademann, R. R. Lucchese and M. J. J. Vrakking, *J. Phys. B At. Mol. Opt. Phys.*, 2012, **45**, 74016.

41 P. Billaud, M. Géléoc, Y. J. Picard, K. Veyrinas, J. F. Hergott, S. Marggi Poullain, P. Breger, T. Ruchon, M. Roulliay, F. Delmotte, F. Lepetit, A. Huetz, B. Carré and D. Dowek, *J. Phys. B At. Mol. Opt. Phys.*, 2012, **45**, 194013.

42 A. Fischer, A. Sperl, P. Cörlin, M. Schönwald, H. Rietz, A. Palacios, A. González-Castrillo, F. Martín, T. Pfeifer, J. Ullrich, A. Senftleben and R. Moshammer, *Phys. Rev. Lett.*, 2013, **110**, 213002.

43 A. Stolow, *Faraday Discuss.*, 2013, **163**, 9–32.

44 A. Ferré, A. E. Boguslavskiy, M. Dagan, V. Blanchet, B. D. Bruner, F. Burgy, A. Camper, D. Descamps, B. Fabre, N. Fedorov, J. Gaudin, G. Geoffroy, J. Mikosch, S. Patchkovskii, S. Petit, T. Ruchon, H. Soifer, D. Staedter, I. Wilkinson, A. Stolow, N. Dudovich and Y. Mairesse, *Nat. Commun.*, 2015, **6**, 5952.

45 M. Lebech, J. C. Houver, A. Lafosse, D. Dowek, C. Alcaraz, L. Nahon and R. R. Lucchese, *J. Chem. Phys.*, 2003, **118**, 9653–9663.

46 D. Dowek and R. R. Lucchese, in *Dynamical Processes in Atomic and Molecular Physics*, Bentham, Bussum, The Netherlands, 2012, pp. 57–95.

47 A. Lafosse, M. Lebech, J. C. Brenot, P. M. Guyon, O. Jagutzki, L. Spielberger, M. Vervloet, J. C. Houver and D. Dowek, *Phys. Rev. Lett.*, 2000, **84**, 5987–5990.

48 M. Lebech, J. C. Houver and D. Dowek, *Rev. Sci. Instrum.*, 2002, **73**, 1866–1874.

49 W. B. Li, R. Montuoro, J. C. Houver, L. Journel, A. Haouas, M. Simon, R. R. Lucchese and D. Dowek, *Phys. Rev. A*, 2007, **75**, 52718.

50 R. R. Lucchese, A. Lafosse, J. C. Brenot, P. M. Guyon, J. C. Houver, M. Lebech, G. Raseev and D. Dowek, *Phys. Rev. A*, 2002, **65**, 20702.

51 D. Dowek, M. Lebech, J. C. Houver and R. R. Lucchese, *Mol. Phys.*, 2007, **105**, 1757–1768.

52 S. J. Weber, B. Manschwetus, M. Billon, M. Böttcher, M. Bougeard, P. Breger, M. Géléoc, V. Gruson, A. Huetz, N. Lin, Y. J. Picard, T. Ruchon, P. Salières and B. Carré, *Rev. Sci. Instrum.*, 2015, **86**, 33108.

53 P. Antoine, A. L'Huillier, M. Lewenstein, P. Salières and B. Carré, *Phys. Rev. A*, 1996, **53**, 1725–1745.

54 H. Ruf, C. Handschin, R. Cireasa, N. Thiré, A. Ferré, S. Petit, D. Descamps, E. Mével, E. Constant, V. Blanchet, B. Fabre and Y. Mairesse, *Phys. Rev. Lett.*, 2013, **110**, 83902.

55 M. Gisselbrecht, A. Huetz, M. Lavollée, T. J. Reddish and D. P. Seccombe, *Rev. Sci. Instrum.*, 2005, **76**, 13105.

56 O. Guyétand, M. Gisselbrecht, A. Huetz, P. Agostini, B. Carré, P. Breger, O. Gobert, D. Garzella, J.-F. Hergott, O. Tcherbakoff, H. Merdji, M. Bougeard, H. Rottke, M. Böttcher, Z. Ansari, P. Antoine and L. F. DiMauro, *J. Phys. B At. Mol. Opt. Phys.*, 2008, **41**, 65601.

57 P. Hockett, C. Z. Bisgaard, O. J. Clarkin and A. Stolow, *Nat. Phys.*, 2011, **7**, 612–615.

58 F. Martin, J. Fernandez, T. Havermeier, L. Foucar, T. Weber, K. Kreidi, M. Schoffler, L. Schmidt, T. Jahnke, O. Jagutzki, A. Czasch, E. P. Benis, T. Osipov, A. L. Landers, A. Belkacem, M. H. Prior, H. Schmidt-Bocking, C. L. Cocke and R. Dorner, *Science*, 2007, **315**, 629–633.

59 D. Dowek, J. F. Pérez-Torres, Y. J. Picard, P. Billaud, C. Elkharrat, J. C. Houver, J. L. Sanz-Vicario and F. Martín, *Phys. Rev. Lett.*, 2010, **104**, 233003.

60 A. Lafosse, J. C. Brenot, A. V. Golovin, P. M. Guyon, K. Hoejrup, J. C. Houver, M. Lebech and D. Dowek, *J. Chem. Phys.*, 2001, **114**, 6605–6617.

61 K. Veyrinas, PhD Thesis, Université Paris-Sud 11, U.F.R. Scientifique d'Orsay, 2015.

62 In preparation.

63 Y. Iida, F. Carnovale, S. Daviel and C. E. Brion, *Chem. Phys.*, 1986, **105**, 211–225.

64 R. E. Stratmann, R. W. Zurales and R. R. Lucchese, *J. Chem. Phys.*, 1996, **104**, 8989–9000.

65 B. Manschwetus, N. Lin, J. Rothhardt, R. Guichard, T. Auguste, A. Camper, P. Breger, J. Caillat, M. Géléoc, T. Ruchon, R. Taïeb, B. Carré and P. Salières, *J. Phys. Chem. A*, 2015, **119**, 6111–6122.

66 A.-T. Le, R. R. Lucchese and C. D. Lin, *Phys. Rev. A*, 2013, **87**, 63406.

67 R. Torres, N. Kajumba, J. G. Underwood, J. S. Robinson, S. Baker, J. W. G. Tisch, R. de Nalda, W. A. Bryan, R. Velotta, C. Altucci, I. C. E. Turcu and J. P. Marangos, *Phys. Rev. Lett.*, 2007, **98**, 203007.

68 O. Smirnova, S. Patchkovskii, Y. Mairesse, N. Dudovich, D. Villeneuve, P. Corkum and M. Y. Ivanov, *Phys. Rev. Lett.*, 2009, **102**, 63601.

69 M. C. H. Wong, A.-T. Le, A. F. Alharbi, A. E. Boguslavskiy, R. R. Lucchese, J.-P. Brichta, C. D. Lin and V. R. Bhardwaj, *Phys. Rev. Lett.*, 2013, **110**, 33006.

70 M. Negro, M. Devetta, D. Faccialá, S. D. Silvestri, C. Vozzi and S. Stagira, *Faraday Discuss.*, 2014, **171**, 133–143.

71 L. Nahon, G. A. Garcia and I. Powis, *J. Electron Spectrosc. Relat. Phenom.*, 2015, **204**, 322–334.

72 J. Jose, R. R. Lucchese and T. N. Rescigno, *J. Chem. Phys.*, 2014, **140**, 204305.

73 D. Toffoli, R. R. Lucchese, M. Lebech, J. C. Houver and D. Dowek, *J. Chem. Phys.*, 2007, **126**, 54307.

74 S. Marggi Poullain, C. Elkharrat, W. B. Li, K. Veyrinas, J. C. Houver, C. Cornaggia, T. N. Rescigno, R. R. Lucchese and D. Dowek, *J. Phys. B At. Mol. Opt. Phys.*, 2014, **47**, 124024.

75 A.-T. Le, R. R. Lucchese, M. T. Lee and C. D. Lin, *Phys. Rev. Lett.*, 2009, **102**, 203001.

76 A.-T. Le, R. R. Lucchese, S. Tonzani, T. Morishita and C. D. Lin, *Phys. Rev. A*, 2009, **80**, 13401.

77 P. Salières, A. Maquet, S. Haessler, J. Caillat and R. Taïeb, *Rep. Prog. Phys.*, 2012, **75**, 62401.